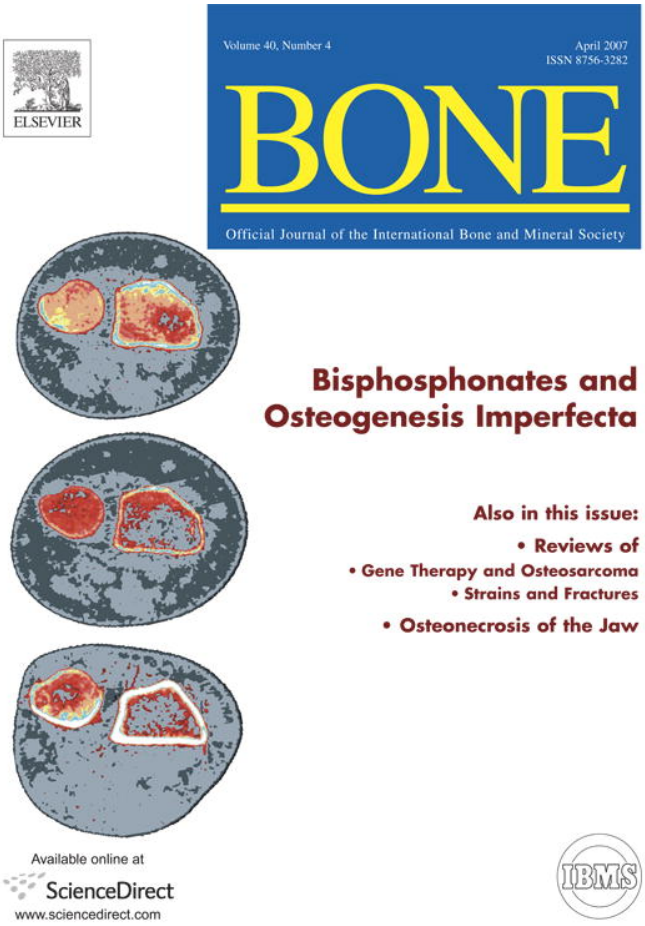

ELSEVIER

Bone 40 (2007) 904 – 912

BONE

www.elsevier.com/locate/bone

Evaluation of bioreactor-cultivated bone by magnetic resonance microscopy and FTIR microspectroscopy

Ingrid E. Chesnick [a], Francis A. Avallone [b], Richard D. Leapman [c], William J. Landis [d], Naomi Eidelman [e], Kimberlee Potter [a,*]

[a] *Magnetic Resonance Microscopy Facility, Department of Biophysics, Armed Forces Institute of Pathology Annex, 1413 Research Blvd, Rockville, MD 20850, USA*

[b] *Department of Genitourinary Pathology, Armed Forces Institute of Pathology, Washington, DC, USA*

[c] *National Institute of Biomedical Imaging and Bioengineering, National Institutes of Health, Bethesda, MD, USA*

[d] *Department of Microbiology, Immunology, and Biochemistry, Northeastern Ohio Universities College of Medicine, Rootstown, OH, USA*

[e] *Paffenbarger Research Center, American Dental Association Foundation, National Institute of Standards and Technology, Gaithersburg, MD, USA*

Received 21 July 2006; revised 23 October 2006; accepted 25 October 2006
Available online 15 December 2006

Abstract

We present a three-dimensional mineralizing model based on a hollow fiber bioreactor (HFBR) inoculated with primary osteoblasts isolated from embryonic chick calvaria. Using non-invasive magnetic resonance microscopy (MRM), the growth and development of the mineralized tissue around the individual fibers were monitored over a period of 9 weeks. Spatial maps of the water proton MRM properties of the intact tissue, with 78 μm resolution, were used to determine changes in tissue composition with development. Unique changes in the mineral and collagen content of the tissue were detected with high specificity by proton density (PD) and magnetization transfer ratio (MTR) maps, respectively. At the end of the growth period, the presence of a bone-like tissue was verified by histology and the formation of poorly crystalline apatite was verified by selected area electron diffraction and electron probe X-ray microanalysis. FTIR microspectroscopy confirmed the heterogeneous nature of the bone-like tissue formed. FTIR-derived phosphate maps confirmed that those locations with the lowest PD values contained the most mineral, and FTIR-derived collagen maps confirmed that bright pixels on MTR maps corresponded to regions of high collagen content. In conclusion, the spatial mapping of tissue constituents by FTIR microspectroscopy corroborated the findings of non-invasive MRM measurements and supported the role of MRM in monitoring the bone formation process *in vitro*.

Keywords: Bone; Bioreactor; Collagen; Mineral; Magnetic resonance microscopy; FTIR microspectroscopy

Introduction

There are numerous examples in the literature of tissue-engineered bone constructs composed of primary calvarial osteoblasts or bone marrow stem cells seeded onto a variety of scaffold materials [1,2]. Typically, constructs are grown under perfusion conditions either in a columnar [3] or rotating bioreactor [4] to promote the formation of bone throughout the scaffold. A better understanding of the regulatory role of various endogenous growth factors and mechanical loading conditions could greatly improve the quality of bioreactor-derived bone [5]. Therefore, to study the impact of various biochemical and biomechanical factors on the bone formation process, we have developed a three-dimensional (3D) mineralizing culture system using a hollow fiber bioreactor (HFBR) system. The HFBR system is inoculated with primary osteoblasts and the tissue formed by the cells is interrogated spatially and temporally by proton magnetic resonance microscopy (MRM). This model system will facilitate the study of different therapeutic interventions on the bone formation process.

The advantage of a HFBR system is that it can support high cell densities, which are thought to be necessary for the

* Corresponding author. Fax: +1 301 295 9507.
E-mail address: potterk@afip.osd.mil (K. Potter).

8756-3282/$ - see front matter © 2006 Elsevier Inc. All rights reserved.
doi:10.1016/j.bone.2006.10.020

functional development of bone cells [6]. In addition, the continuous perfusion of the cells attached to the fiber surface will promote the appositional growth of bone in the radial direction, resulting in more mineralized tissue compared to monolayer cultures or cells seeded onto highly porous polymer meshes cultured under static conditions [3,7]. Lastly, bone cells are expected to thrive within the HFBR system because the cells experience fluid shear stresses [3,7–11]. The drawback of this HFBR system is the inability to sample the tissue as it forms in the reactor. It is for this reason we monitored the mineralization process with MRM.

Unlike conventional techniques such as histomorphometry, X-ray diffraction, and scanning and transmission electron microscopy, MRM can be performed without destructive preparative techniques. However, because of the limited resolution of the MRM technique it cannot resolve individual cells found in the mineralized tissue. Therefore, spatial maps of MRM properties of the intact tissue are used to ascertain its composition. Using this approach, unique changes in collagen and mineral content can be detected with high specificity, which in turn can be used to monitor the mineralization process indirectly. MRM can also be used to measure the amount and spatial localization of additional tissue properties such as hydration state and lipid content [12]. This non-invasive methodology has been adopted to examine bone formation in various tissue-engineering applications [12–14].

Typically, proton MRM images of cortical bone yield very little signal as a result of its low water content. Consequently, images of cortical bone must be acquired using solid-state imaging techniques to detect the ^{31}P nuclei immobilized in the inorganic matrix [15–19] or the ^{1}H nuclei in bone water [20,21]. In mineralizing systems, the tissues are still mostly hydrated and the reduction in the water proton signal can be attributed to the displacement of water by mineral deposits containing few mobile protons, and thus proton images of tissue water can be inversely related to its mineral content [12]. In contrast, for a developing system the ^{31}P signal of bone is not very large owing to the exceedingly small amounts of mineral deposited, which can be overwhelmed by contributions from the phosphate ions present in the culture medium, phosphorylated cytosolic metabolites, and membrane phospholipids [22].

MRM can also be used to evaluate the collagen content of tissues because collagen gives rise to a significant magnetization transfer (MT) effect [23,24]. The MT effect is the result of cross-relaxation between mobile water protons and the less mobile hydroxyl groups on the collagen molecules [25,26]. In fact, calibration curves have been derived for this MRM parameter and the collagen content of articular cartilage [27], engineered cartilage [28], and collagen gels [27,29,30]. In this mineralizing system, collagen, the predominant organic constituent of bone, was assessed using MT ratio images [12,13,31,32].

To confirm the presence of bone within our HFBR system, we subjected the tissue to FTIR microspectroscopy. The utility of FTIR microspectroscopy in studying mineralized tissues is well established [33–36]. The technique combines histology-like spatial localization with the quantitative capability of bulk chemical analysis and it is used routinely in such specimens to assess the spatial distribution of mineral and collagen (from the phosphate and amide peaks, respectively) [37,38]. It also provides information about mineral crystallinity as a function of spatial location in a sample such as the growth plate of a rat [39] or at distances from an osteon in human bone [40] or from the dentin–enamel junction in the human tooth [41].

In this study, we described an HFBR system for growing bone and demonstrate its capacity to generate bone-like tissue on the surface of the hollow fibers. The occurrence of bone in the bioreactor was established by histology. Electron diffraction, in conjunction with X-ray microanalysis, confirmed that the mineral formed was poorly crystalline apatite. MRM images of the bioreactor in cross-section confirmed the presence of a dehydrated collagen-containing tissue around the fibers, which on further analysis by FTIR microspectroscopy was found to have similar composition to that of bone. We also present the utility of the MRM technique to track spatial and temporal changes as the mineralized tissue is formed.

Methods

Mineralizing bioreactor

Our mineralizing model is based on an HFBR design, previously described for chondrocytes [42], in which culture medium flows through the lumen of hollow fibers and osteoblasts attach to their outer surfaces. The bioreactors were constructed from high-purity glass tubing (o.d. 5 mm, height 50 mm) with a sideport for the injection of cells into the extracapillary space. Each reactor had seven porous polypropylene (PP) hollow fibers (i.d. 330 μm, pore diameter 0.2 μm, wall thickness 150 μm; Microgon, Inc., Laguna Hills, CA) potted with biomedical grade silicone rubber (MED-1137, Nusil Silicone Technology, Carpenteria, CA). The bioreactors were pre-treated with 100% ethanol to enhance the wettability of the fibers, washed with distilled water to remove the ethanol, and autoclaved while immersed in water to prevent excessive heating of the PP fibers.

Each bioreactor was connected to a 100-mL reservoir bottle by 10 ft. of gas permeable silicone tubing (Cole Parmer, Vernon Hills, IL) and unidirectional flow was achieved by a compressible pump interface with one-way flow valves on either side. Prior to connecting to the HFBR, the flow circuit was autoclaved and flushed with tissue culture medium. The whole assembly was attached to a compression pump (FiberCell Systems, Inc., Frederick, MD) and maintained in a 5% CO_2 incubator for a minimum of 2 days before inoculation with cells to ensure the sterility and integrity of the system.

Cell inoculation

Primary osteoblasts were obtained from the third population of cells released by serial collagenase digestion of the calvarial bones of 16-day-old embryonic chicks [43]. Cells were harvested with the approval and strict adherence to the guidelines of the Institutional Animal Care and Use Committee at the Armed Forces Institute of Pathology. For the final digest, minced calvaria were treated with 3 mg/mL collagenase (Roche Molecular Biochemicals, Indianapolis, IN) for 30 min at 37°C with agitation. Isolated osteoblasts were resuspended in tissue culture medium, and each bioreactor was inoculated with 10^7 cells using a syringe inserted through the rubber septa on the sideport. Perfusion of the HFBR was delayed by 1–2 h to facilitate adhesion of the cells to the fibers. The flow rate of the culture medium was increased gradually over the period of a week from 3 mL/min to 14 mL/min.

Tissue culture medium was prepared by adding 50 mL of heat-inactivated fetal bovine serum (Biofluids, Rockville, MD), 5 mL of 200 mM L-glutamine (Biofluids), 0.5 mL of 250 μg/mL fungizone (Biofluids), and 0.5 mL of 10 mg/mL gentamicin reagent solution (Gibco, Gaithersburg, MD) to a 500-mL bottle of Dulbecco's modified Eagle's medium (Biofluids). Ascorbic acid

(Sigma, St. Louis, MO) was added at each medium change, twice per week, such that its final concentration was 50 μg/mL. After 1 week of growth, tissue culture medium in the reservoir bottle (40 mL) was supplemented with 1 mL of 46 mM β-glycerophosphate (Sigma, St. Louis, MO), an organic phosphate source.

Magnetic resonance microscopy

All MRM images were acquired with a Bruker DMX spectrometer (Bruker BioSpin Corp., Billerica, MA) coupled to a wide-bore magnet (dia. 89 mm) operating at 9.4 T (400.13 MHz for protons). Bioreactors, including connecting tubing, were imaged in a 25-mm diameter radiofrequency probe. During image acquisition the bioreactor was maintained under incubator-like conditions (37°C and 5% CO_2). A pump, under spectrometer control, was used to regulate fluid flow during image acquisition and eliminate image artifacts caused by flow effects. These precautions guaranteed that the changes observed in MRM images were attributable to tissue-level changes and not to environmental changes or imaging artifacts.

Pilot images, acquired perpendicular to the long axis of the HFBR, were used to locate the ideal slice location, and cross-sectional images were acquired with a slice thickness of 1 mm and an in-plane spatial resolution of 78 μm. Typically, MRM images were acquired from the same slice location each week for up to 9 weeks. Quantitative T2 relaxation and proton density (PD) maps were calculated from the fit of 16 images acquired with a multiecho sequence using a long repeat time (TR = 5 s) and echo times (TE) between 10 and 160 ms. MTR maps were calculated using the following equation: $[1 - M_{so}/M_o]$, where M_{so}/M_o is defined as the ratio of image intensities acquired with and without the application of a 5-s, 12-μT saturation pulse, 6000 Hz off-resonance [27]. All image analysis was performed using Bruker Paravision software as well as user-defined procedures in IDL (Interactive Data Language, ITT Visual Information Solutions, Boulder, CO).

To assess temporal changes in tissue MRM parameters, we used a region-growing segmentation tool to establish Region 1, the tissue around fibers 1, 2, and 3, and Region 2, the tissue around fibers 4, 5, 6, and 7 (see Fig. 3). Typically, a seed point was selected within the region-of-interest and a region was grown until an intensity criterion for stopping growth was met. Spatially averaged intensities were used to calculate the T2 and PD values for Regions 1 and 2. The hydration state of the two tissue zones was calculated by normalizing the PD value for the tissue against the PD value measured for the surrounding medium. Spatially averaged MRM parameters are more accurate because the data to be fitted have higher signal-to-noise ratios compared to individual pixels. However, the reported standard deviations do not reflect the spatial heterogeneity of the tissue, but rather the standard deviations of the fitted parameters. Notably, the error for spatially averaged MTR values was significant owing to the variability in data caused by the heterogeneity of the tissue and the additive effect on the errors when two numbers are divided. Consequently, we estimated the variability in the MTR measurement for each region by averaging together multiple measurements made using different seed points.

After the last MRM measurements, HFBRs were disconnected from the flow circuit and flushed with cryo-sectioning embedding material (OCT Tissue-Tek, Miles, Inc., Elkhart, IN) to remove residual tissue culture medium in the lumen of the fibers and in the extracapillary space. The glass ends of the reactor were scored with a tungsten carbide blade and cracked open without severing the fibers and the entire assembly was frozen. The fibers at the outflow end were cut with a razor blade and the fibers plus OCT matrix were removed from the glass body of the reactor. The section of the reactor corresponding to the 1-mm slab of material imaged by MRM was excised and cryo-sectioned on a Minotome Plus cryostat (Triangle Biomedical Sciences, Atlanta, GA).

FTIR microspectroscopy

Cryo-sections (~8 μm thick) of HFBR tissue were placed on low-emissivity reflective glass slides (Kevley Technologies, Chesterland, OH) and stored in a desiccant dryer prior to being analyzed by FTIR reflectance-transmission microspectroscopy (FTIR-RTM) mapping [44,45]. The low-emissivity highly reflective slides were used because their mirror-like coating reflects the infrared beam back through the thin section to yield reflection-transmission spectra, which are equivalent to "normal" absorption spectra after transforming them to absorbance without any mathematical correction [44–46]. The FTIR-RTM measurements were performed with a Nicolet Magna-IR 550 FTIR spectrophotometer interfaced to a Nic Plan microscope (Thermo Nicolet, Inc., Madison, WI). The microscope was equipped with a video camera and a liquid nitrogen cooled mercury–cadmium–telluride (MCT) detector (Thermo Nicolet). The sections were mapped using a computer-controlled microscope stage (Spectra-Tech, Inc., Shelton, CT), programmable in the x and y directions, and Atlμs Microscope mapping software (Thermo Nicolet). The spectra were recorded at a spectral resolution of 8 cm^{-1} with 16 to 256 co-added scans collected in the range of [650 to 4000] cm^{-1}, using a 20×20 μm^2 or larger aperture. All spectra were ratioed against the background spectrum collected from a bare spot in the reflective slide. The spectra were transformed to absorbance without any mathematical correction [44] and baseline-corrected from [750 to 1770] cm^{-1}. The FTIR-RTM maps were processed as color contour maps of collagen (area under the Amide I and II peaks in the [1500 to 1690] cm^{-1} spectral region) and mineral (area under the ν_3PO_4 bands at the [750 to 1195] cm^{-1} spectral region).

Fine powders of synthetic apatite and bone were embedded in spectroscopic grade KBr and pressed into pellets (13 mm diameter, 1 mm thick). IR spectra were collected from the pellets from [400 to 4000] cm^{-1} at a resolution of 2 cm^{-1} with 256 co-added scans using the Nicolet Magna-IR 550 FTIR spectrophotometer continuously purged with dry air. The synthetic apatite, prepared under physiological conditions (37°C and pH 7.4), was donated by Dr. E. D. Eanes (Mineral Chemistry and Structure Section, National Institute of Dental and Craniofacial Research, NIH). The fine powdered cow bone was donated by Mr. B. O. Fowler (Mineral Chemistry and Structure Section, National Institute of Dental and Craniofacial Research, NIH).

Histology

The mineralized tissue deposited on the PP fibers was fixed by introducing neutral buffered formalin into the extracapillary space of the reactor. After fixation, the body of the reactor was filled with low melting point agarose (~1% w/v) and the fibers plus gel were removed from the glass body of the reactor as described previously. The fibers encased in gel were embedded in paraffin and sectioned (~5 μm thickness) perpendicular to the long axis of the bioreactor. Contiguous sections were stained with Alizarin red and von Kossa, which stain calcium (red) and phosphate (black), respectively [47].

Scanning electron microscopy

Specimens were critical point dried through ethanol, sputter-coated with a thin layer of carbon, and examined using a JEOL model JSM 35U (JEOL USA, Peabody, MA) scanning electron microscope operated at 25 kV.

Mineral characterization

Bioreactor fibers were dehydrated with ethylene glycol (Sigma) and embedded in LR White resin (EF Fullam, Inc., Latham, NY), thin sectioned (~80 nm) on a Reichert Ultracut S ultramicrotome (Leica, Deerfield, IL), floated briefly on a microtome trough of double distilled water (pH >8), mounted on copper grids, and left unstained [48]. Thin sections were examined by electron microscopy at a beam voltage of 120 kV with a CM120 transmission electron microscope (FEI, Eindhoven, The Netherlands) equipped with an Oxford Pentafet energy-dispersive X-ray detector (Oxford Instruments, High Wycombe, UK) and a GIF100 imaging filter (Gatan, Inc., Pleasanton, CA) [49].

TEM images were used to locate mineral deposits and the mineral, in 1-μm diameter areas of the specimen, was subjected to selected area electron diffraction (SAED). Diffraction patterns and TEM images were recorded digitally using a CCD camera controlled by Gatan Digital Micrograph v.3.3 software (Gatan, Inc.) running on a Power Macintosh computer. All but zero-loss electrons were energy-filtered from the diffraction pattern to remove the background intensity caused by multiply scattered electrons [50]. The focal length of the microscope in diffraction mode was calibrated with a grid of evaporated gold (EF Fullam, Inc.) and the diameters of observed polycrystalline ring patterns were measured using NIH IMAGE software (http://rsb.info.nih.gov/nih-image/) [51]. After collection of diffraction data, energy-dispersive X-

ray spectra were acquired for the same mineral deposits examined by SAED with the electron beam focused to a diameter of ~0.5 μm and acquisition times between 50 and 100 s. Quantitative microanalysis was performed using the NIST/NIH Desktop Spectrum Analyzer (DTSA) [52]. Peak areas of emission lines were quantitated by Simplex curve fitting and atomic ratios of Ca:P were obtained using the calculated relative efficiency factors for Ca and P X-ray production and detection.

Results

Mineralizing bioreactor

Photographs of a representative hollow fiber bioreactor 4 weeks after inoculation are shown in Fig. 1. An Alizarin red-stained section (Fig. 1B) shows two PP fibers from the bioreactor. The tissue growing on the surface of the fibers stained red, confirming the presence of calcium. Sections treated by von Kossa staining were imparted with black color (data not shown), a result indicating the presence of phosphate within the tissue. Taken together, the common staining by Alizarin red and von Kossa demonstrates mineral deposition in the tissue developed in the bioreactors. A scanning electron micrograph (Fig. 1C) illustrates the attachment of osteoblasts to the relatively smooth surface of PP fibers extracted from the reactor shown in Fig. 1A. Osteoblasts overlying a matrix of mineralized collagen fibers can be observed at higher resolution in Fig. 1D.

Mineral characterization

To confirm the crystallographic nature of the mineral deposits formed in the HFBR system, we subjected mineral crystals to electron diffraction and X-ray microanalysis. Tissue sections, such as those shown in the transmission electron micrograph in Fig. 2A, were subsequently subjected to electron diffraction. A representative diffraction pattern from a single mineral deposit is presented in Fig. 2B. The broad outer ring representing the 211, 112, and 300 reflections and the smaller inner ring representing the 002 reflection taken together confirm that the mineral in this sample was poorly crystalline apatite. X-ray spectra were also obtained from unmineralized and mineralized portions of the same mineral deposit characterized by electron diffraction. The X-ray spectra for a translucent matrix site and a dense mineral deposit, in the locations indicated on the transmission image of Fig. 2A, are shown in Figs. 2C and D, respectively. The most prominent peaks in the spectrum from typical unmineralized tissue were those of carbon and oxygen, suggestive of organic matrices such as unmineralized osteoid. For mineralized tissue, the principal peaks in X-ray spectra were those of phosphorus and calcium. The Ca:P ratio of such mineral deposits ($n=7$) was found to range from 1.52 to 1.61.

MRM results

MRM images were acquired at weekly intervals for each bioreactor at a set slice location (see Methods) to establish the exact changes in the MRM properties that occur as the tissue mineralizes. Images from one such bioreactor are presented in Fig. 3. Each image represents a 1-mm slice taken perpendicular to the fiber axis, approximately 12 mm from the sideport near the outflow of the bioreactor, with a nominal in-plane resolution of 78 μm. Selected proton density (top) and MTR (bottom) images in Fig. 3 were acquired at 4 (A, E), 6 (B, F), 7 (C, G), and 9 (D, H) weeks after the bioreactor was inoculated with cells. Each fiber was surrounded by tissue, which was less hydrated (or darker) than the surrounding culture medium on PD maps. Zones with the lowest PD values, for example between fibers 1 and 2 and in the intervening space between fibers 5, 6, and 7, are expected to have the highest mineral content. Notably, there was an apparent increase in the area of mineralized tissue observed on proton density maps (Figs. 3A–D), a result consistent with more mineral formation with increasing time in culture.

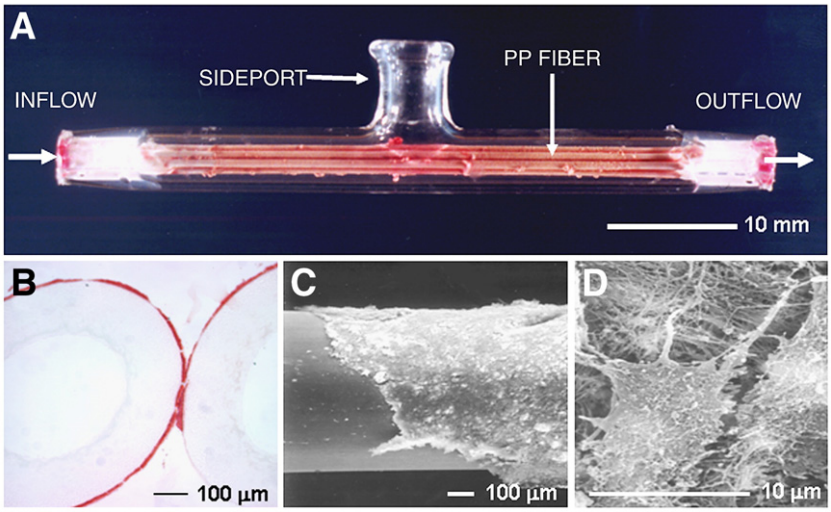

Fig. 1. (A) Photograph of a hollow fiber bioreactor 4 weeks after inoculation with 10^7 primary osteoblasts and subsequent critical-point drying of its contents. Small mineral deposits were observed on polypropylene (PP) fibers stained with Alizarin red (B) and scanning electron micrographs (C and D) confirmed the attachment of osteoblasts to the PP fibers extracted from the reactor.

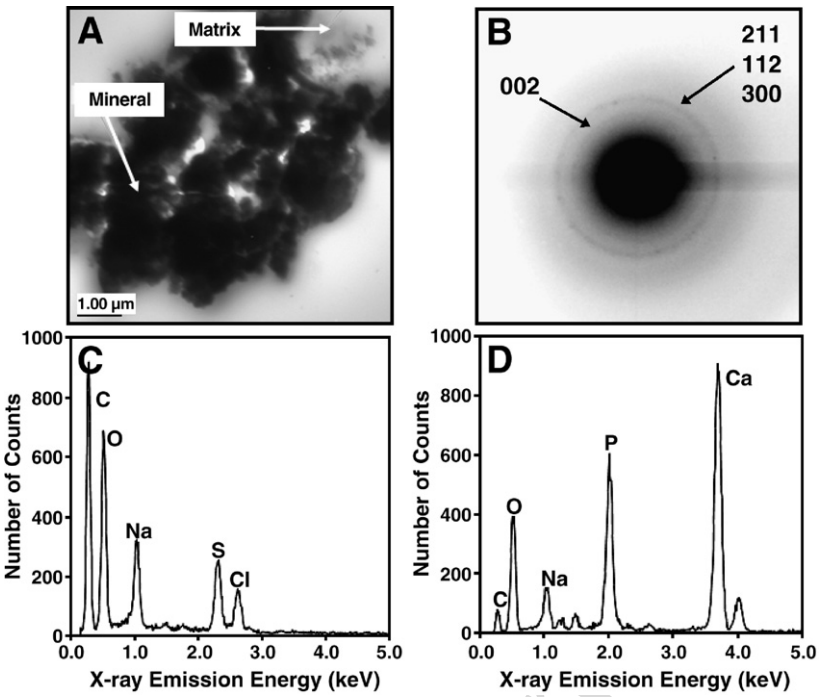

Fig. 2. (A) Transmission electron micrograph of mineralized tissue from a HFBR prepared using anhydrous techniques, sectioned ~80 nm thick, and left unstained. Mineralized zones appear dark and unmineralized matrix appears translucent in the transmission image (scale bar=1 μm). (B) Selected area diffraction pattern (120 kV) of mineral from the location labeled "mineral" on the TEM image. Reflections are indicative of poorly crystalline apatite. (C and D) X-ray energy spectra of unmineralized and mineralized tissue, respectively. Phosphorus and calcium dominate the mineralized tissue spectrum, and carbon and oxygen are prominent in the unmineralized matrix spectrum.

Newly formed tissue, containing measurable quantities of collagen, was visible on MTR maps (Figs. 3E–H). By 4 weeks much of the tissue surrounding the fibers contained collagen, indicative of newly deposited osteoid tissue. More importantly, in the heavily mineralized zones of the bioreactor, the MTR values were higher than the adjacent tissue. With longer culture times, the MTR values of the tissue surrounding the fibers and the heavily mineralized zones slowly decreased. In some mineralized locations, the MTR values were indeterminate because of the very low image intensities in those regions.

To assess more completely how the MRM properties of the developing tissue change with increasing time in culture, we extracted spatially averaged MRM parameters for two regions of tissue in one bioreactor. Region 1 was composed of tissue around fibers 1, 2, and 3 and Region 2 was composed of tissue around fibers 4, 5, 6, and 7. In Fig. 4, we present the spatially

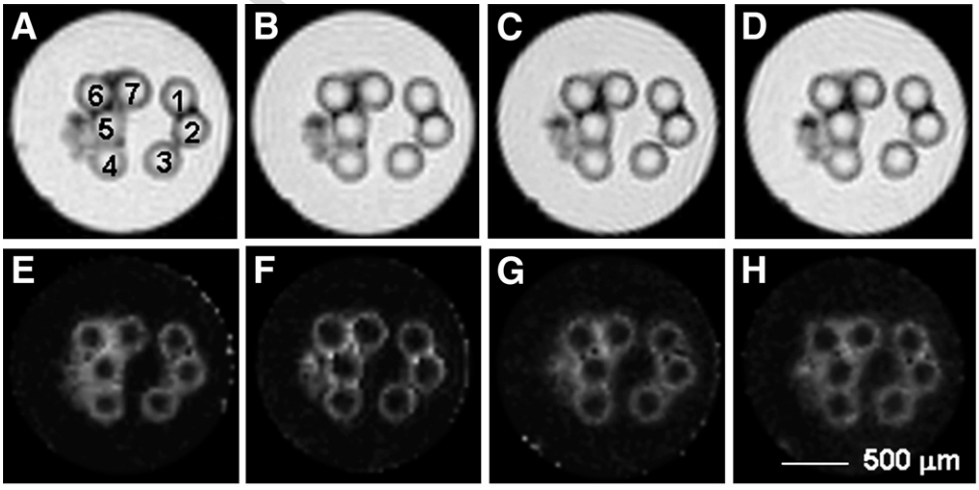

Fig. 3. Representative MRM images of a single bioreactor acquired at 4 (A, E), 6 (B, F), 7 (C, G), 9 (D, H) weeks post-inoculation. Proton density (top row) and MTR (bottom row) maps represent a 1-mm slice of tissue taken perpendicular to the fiber axis and at approximately the same location for each time point. Images had a nominal in-plane resolution of 78 μm. Dark regions on proton density maps correspond to heavily mineralized tissue. Scale bar=500 μm.

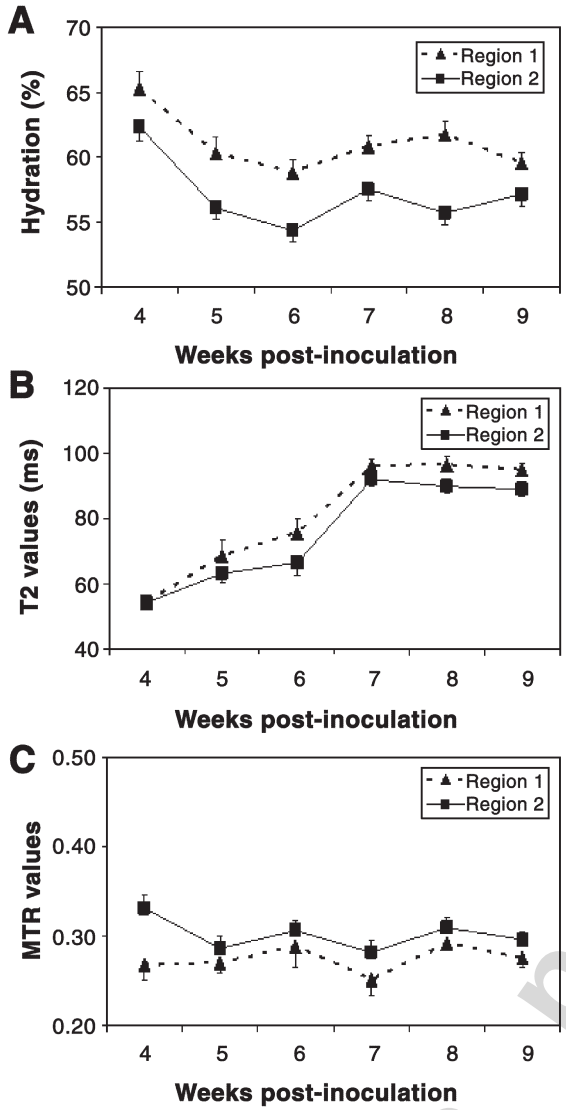

Fig. 4. Spatially averaged values for tissue hydration (A), T2 (B), and MTR (C) values for tissue around fibers 1, 2, and 3 (Region 1, triangles connected with a dashed line) and for tissue around fibers 4, 5, 6, and 7 (Region 2, squares connected with a solid line) measured at weekly intervals.

averaged tissue hydration (A), T2 (B), and MTR (C) values for Regions 1 and 2 as a function of time in culture. Data presented in the graphs in Fig. 4 are for all inclusive weeks starting at week 4 and ending at week 9.

Overall, the tissue in Region 1 was more hydrated with higher T2 values and lower MTR values compared to the tissue in Region 2. More importantly, there were definite trends in the MRM parameter data. Between weeks 4 and 6, the hydration state for both tissue zones steadily decreased with a concomitant increase in T2 values. MTR values decreased from weeks 4 to 5 but peaked slightly by week 6. By week 7, the hydration state of both tissue zones increased resulting in higher T2 and lower MTR values. By week 8, the hydration state of Region 2 had decreased while the hydration state of Region 1 increased slightly compared to the previous week. The lower hydration state for Region 2 tissue resulted in a small reduction in T2 and a slight increase in its MTR value. In Region 1, the slightly higher hydration state did not impact the T2 of the tissue but its MTR value was somewhat increased. By week 9, the hydration state in Region 1 was reduced compared to week 8, resulting in slightly lower T2 and MTR values. In Region 2, the hydration state had increased and the T2 and MTR values were reduced compared to the previous week.

FTIR results

Representative PD and MTR maps, acquired for the HFBR shown in Fig. 3 (9 weeks post-inoculation), are shown in Figs. 5A and B, respectively. The zones with the lowest PD values (dark zones in Fig. 5A) were found to contain the most mineral on the FTIR-derived phosphate map (Fig. 5C). The FTIR-derived collagen map (Fig. 5D) confirmed that bright pixels on the MTR map (Fig. 5B) corresponded to regions of high collagen content. The similar appearances of the color contours on both the FTIR-derived phosphate (Fig. 5C) and collagen (Fig. 5D) maps indicate that both collagen and mineral were co-localized.

The visible image of the HFBR cross-section and selected enlarged images obtained with the FTIR microscope from different mineralized regions are shown in Figs. 5E–I. The highly porous, mineralized tissue between fibers 5, 6, and 7 (shown in Fig. 5G) resembles woven bone and the FTIR spectrum extracted from that location (spectrum G in Fig. 5J) confirmed the presence of bone-like tissue in that zone. Representative FTIR spectra, extracted from those locations indicated on the enlarged views in Figs. 5F–I and presented in Fig. 5J, were compared to spectra of OCT embedding matrix, PP fiber wall, powdered cow bone, and synthetic apatite.

Spectra F, G, and H were comparable to that of the reference bone spectrum and the mineral region (ν_3PO_4, [980 to 1200] cm^{-1}) was similar to that of apatite prepared under physiological conditions without carbonate. The ν_1PO_4 band at ~960 cm^{-1} can be seen in spectra F, G, and H. However, the ν_3PO_4 region in spectrum F was truncated as a result of the high mineral content of this region, which resulted in saturation of the FTIR detector. The ν_3CO_3 type B bands at ~1415 cm^{-1}, 1440 cm^{-1}, and ~870 cm^{-1} were apparent in spectra F, G, and H. Overall, FTIR spectra for the tissue between fibers 1 and 2 (Fig. 5F) and in the intervening space between fibers 5, 6, and 7 (Fig. 5G) had a higher mineral content than the tissue located between fibers 6 and 7 (Fig. 5H) or the tissue on the surface of fiber 3 (Fig. 5I).

Discussion

In this work, we present a model mineralizing system based on a HFBR system. Osteoblasts introduced into the extra-capillary space attach to the surface of the fibers and produce a tissue that is bone-like, a result confirmed by histology, transmission and scanning electron microscopy, electron diffraction, and FTIR-RTM. The diffraction pattern for the mineral deposited in the HFBR was comparable to poorly crystalline apatite and its calcium-to-phosphate ratio, deter-

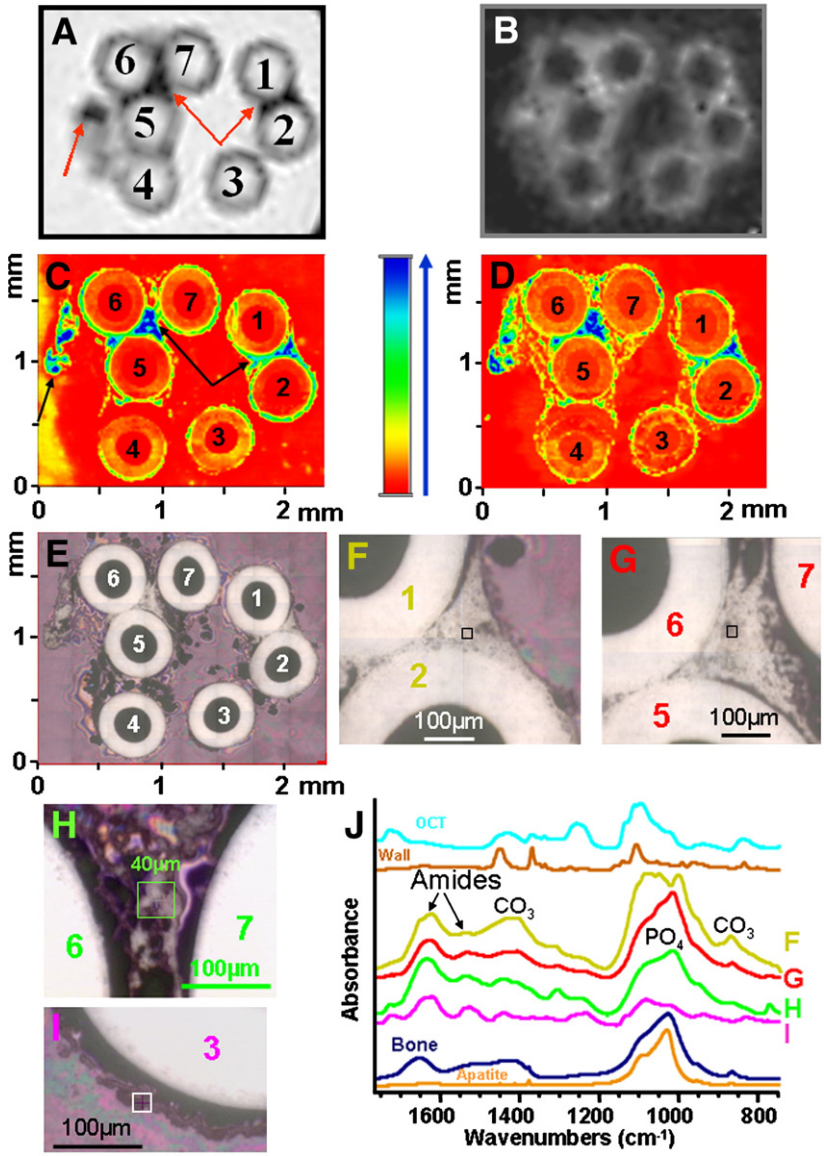

Fig. 5. Proton density (A) and MTR (B) maps of a 9-week HFBR with FTIR-RTM-derived phosphate (C) and collagen (D) maps (low → high values = red → blue). The visual map of the HFBR section (E) and selected enlarged images (F, G, H, I) from different locations were obtained with the FTIR microscope. FTIR spectra from locations indicated in the corresponding images (F, G, H, I) are presented in panel J, along with representative spectra of OCT embedding medium, PP fiber, cow bone, and synthetic apatite. The dimensions of the squares (or spot sizes) in panels F, G, and I are 20 × 20 μm^2. Red arrows in panel A and black arrows in panel C indicate localized mineral deposits.

mined by X-ray microanalysis, was comparable to that reported for bone from chick embryos [48,53].

The temporal evolution of the tissue formed on the surface of the hollow fibers was monitored by MRM. The area of mineralized tissue, visible on PD maps, increased with time in culture. However, the tissue that formed was not spatially homogeneous. There were low intensity areas on PD maps between fibers 1 and 2 and between fibers 5, 6, and 7 consistent with a low water content or high mineral content. According to spatially averaged data obtained here, there was an overall decrease in tissue hydration between weeks 4 and 6 (Fig. 4A). This result suggests that the tissue mineral content increased during this time. We cannot confirm the observed temporal changes in tissue composition, but we can infer what changes had to occur to impact the MRM properties of the tissue.

Zones with the highest mineral content consistently had the highest MTR values. Similar observations have been made for collagen in calcified cartilage [32], in embryonic bone [31], and in a tissue-engineered phalanx model [12]. We attribute this result to an increase in the collagen content of the mineralized zone, possibly brought about by the dehydration of constituent collagen fibrils. As water is replaced by mineral, the collagen fibrils pack together more tightly, resulting in a higher volume density of collagen [54] and thus higher MTR values. These events above could potentially be used to stage the mineral maturation process.

With the accumulation of additional mineral, the proton signal from the tissue is greatly reduced and the MT effect becomes difficult to measure. Thus, as the tissue matures an overall reduction in the MTR value would be expected. Con-

sequently, the MTR value will oscillate between two extremes, the MTR value of newly formed osteoid and that of mineralized osteoid. Such an oscillation was observed for the MTR values measured in Regions 1 and 2 of a typical bioreactor. The downward trend in MTR values is consistent with the averaged contributions of the new tissue and those from more mineralized tissue zones.

The T2 values of Regions 1 and 2 of the sampled bioreactor increased from weeks 4 to 6, while tissue hydration decreased. This result is likely attributable to a loss of proteoglycans just prior to mineral formation [55,56] and explains the T2 of the medium in the extracapillary space at week 4 (88±8 ms) being significantly lower compared to later time points (158±2 ms, weeks 5 to 9). Proteoglycan gels have a high capacity to retain water but their T2 values are inversely dependent on their concentration [28,57]. Consequently, as the proteoglycan content of the osteoid decreased, its water content decreased and its T2 value increased. This result was consistent with the presumed role of acidic molecules during bone formation. Following this phase of proteoglycan decrease, mineral deposits begin to form in the bioreactor system. Further collagen dehydration caused by mineral formation might explain why spatially resolved MTR values peak at week 6.

The changes observed for spatially resolved parameters at week 7 are consistent with the formation of additional osteoid. T2 values were increased because tissue hydration had increased and MTR values were decreased because the collagen content of the osteoid was fairly sparse. In time, as the osteoid mineralized, tissue hydration decreased and MTR values peaked. These results are consistent with the spatially resolved parameters determined at weeks 8 and 9.

For all time points, the hydration state and T2 values for Region 1 were higher than in Region 2. This result can be attributed to the maturation state of the tissue in each region. Essentially, the tissue in Region 1 might be considered less mature than in Region 2 since a lower mineral content is observed for this region on PD maps. The lower MTR value for Region 1 might be attributed to lower collagen content and thus lower mineral content compared to Region 2. Based on these results, the sequence of events that occur during mineral formation can be studied using MRM. To confirm the MRM findings reported in this paper, tissue from HFBRs grown for different lengths of time will have to be subjected to more detailed biochemical and ultrastructural analyses, which are beyond the scope of this paper.

The spatially resolved FTIR-derived phosphate and collagen images confirm the observed regional differences in quantitative MRM maps acquired at week 9. FTIR-derived phosphate maps confirm that those locations with the lowest PD values contain the most mineral, and FTIR-derived collagen maps confirm that bright pixels on the MTR map correspond to regions of high collagen content. Considering that MRM images (Figs. 3 and 5A, B) represent a 1-mm slice of tissue, the correspondence with FTIR images (Figs. 5C, D) for an 8-μm tissue section was excellent. An exact match, however, was difficult to achieve because of the distortion of the tissue and PP fibers during the preparation of tissue sections for FTIR. While spatial distribution maps for mineral and collagen can be obtained and bioreactor tissue formed can be identified as similar to bone, mineral/matrix ratios and crystallinity could not be calculated because the PO_4 region was saturated in the highly mineralized regions as a consequence of using thick cryo-sections.

In summary, we have developed an HFBR system that can support the three-dimensional growth of osteoblasts, the deposition of unmineralized osteoid, and the development of bone mineral. Mineral is comparable to that of normal embryonic vertebrate tissues in its nature as a poorly crystalline apatite and having Ca:P ratios in the range of ~1.5–1.6. The work establishes that MRM measurements can be used to map tissue constituents spatially and temporally and such data can be corroborated with FTIR-RTM. Thus, this investigation supports the use of MRM in monitoring *in vitro* a wide spectrum of critical aspects of the bone formation process of vertebrates.

Acknowledgments

The authors thank Dr. Iren Horkay (National Institute of Child Health and Human Development) for her assistance with the cell isolation procedure and Ms. Jennifer Hillyer (Northeastern Ohio Universities College of Medicine) for the preparation of tissue samples for SEM and TEM studies. This work was supported in part by NIH grants AR51446 (KP) and AR41452 (WJL) and in part by the NIH Intramural Program (RDL).

References

[1] Ishaug SL, Crane GM, Miller MJ, Yasko AW, Yaszemski MJ, Mikos AG. Bone formation by three-dimensional stromal osteoblast culture in biodegradable polymer scaffolds. J Biomed Mater Res 1997;36:17–28.
[2] Crane GM, Ishaug SL, Mikos AG. Bone tissue engineering. Nat Med 1995;1:1322–4.
[3] Bancroft GN, Sikavitsas VI, van den Dolder J, Sheffield TL, Ambrose CG, Jansen JA, et al. Fluid flow increases mineralized matrix deposition in 3D perfusion culture of marrow stromal osteoblasts in a dose-dependent manner. Proc Natl Acad Sci U S A 2002;99:12600–5.
[4] Yu X, Botchwey EA, Levine EM, Pollack SR, Laurencin CT. Bioreactor-based bone tissue engineering: the influence of dynamic flow on osteoblast phenotypic expression and matrix mineralization. Proc Natl Acad Sci U S A 2004;101:11203–8.
[5] Wendt D, Jakob M, Martin I. Bioreactor-based engineering of osteochondral grafts: from model systems to tissue manufacturing. J Biosci Bioeng 2005;100:489–94.
[6] Kale S, Biermann S, Edwards C, Tarnowski C, Morris M, Long MW. Three-dimensional cellular development is essential for ex vivo formation of human bone. Nat Biotechnol 2000;18:954–8.
[7] Sikavitsas VI, Bancroft GN, Mikos AG. Formation of three-dimensional cell/polymer constructs for bone tissue engineering in a spinner flask and a rotating wall vessel bioreactor. J Biomed Mater Res 2002;62:136–48.
[8] Ajubi NE, Klein-Nulend J, Nijweide PJ, Vrijheid-Lammers T, Alblas MJ, Burger EH. Pulsating fluid flow increases prostaglandin production by cultured chicken osteocytes—A cytoskeleton-dependent process. Biochem Biophys Res Commun 1996;225:62–8.
[9] Goldstein AS, Juarez TM, Helmke CD, Gustin MC, Mikos AG. Effect of convection on osteoblastic cell growth and function in biodegradable polymer foam scaffolds. Biomaterials 2001;22:1279–88.
[10] Hsieh YF, Turner CH. Effects of loading frequency on mechanically induced bone formation. J Bone Miner Res 2001;16:918–24.

[11] Vunjak-Novakovic G, Meinel L, Altman G, Kaplan D. Bioreactor cultivation of osteochondral grafts. Orthod Craniofac Res 2005;8:209–18.
[12] Potter K, Sweet DE, Anderson P, Davis GR, Isogai N, Asamura S, et al. Non-destructive studies of tissue-engineered phalanges by magnetic resonance microscopy and X-ray microtomography. Bone 2006;38:350–8.
[13] Washburn NR, Weir M, Anderson P, Potter K. Bone formation in polymeric scaffolds evaluated by proton magnetic resonance microscopy and X-ray microtomography. J Biomed Mater Res 2004;67A:738–47.
[14] Hong L, Peptan IA, Xu H, Magin RL. Nondestructive evaluation of osteogenic differentiation in tissue-engineered constructs. J Orthop Res 2006;24:889–97.
[15] Ackerman JL, Raleigh DP, Glimcher MJ. Phosphorus-31 magnetic resonance imaging of hydroxyapatite: a model for bone imaging. Magn Reson Med 1992;25:1–11.
[16] Moore JR, Garrido L, Ackerman JL. Solid state phosphorus-31 magnetic resonance imaging of bone mineral. Magn Reson Med 1995;33:293–9.
[17] Wu Y, Ackerman JL, Chesler DA, Li J, Neer RM, Wang J, et al. Evaluation of bone mineral density using three-dimensional solid state phosphorus-31 NMR projection imaging. Calcif Tissue Int 1998;62:512–8.
[18] Wu Y, Chesler DA, Glimcher MJ, Garrido L, Wang J, Jiang HJ, et al. Multinuclear solid-state three-dimensional MRI of bone and synthetic calcium phosphates. Proc Natl Acad Sci U S A 1999;96:1574–8.
[19] Gillies DG, Newling B, Randall EW. Phosphorus-31 solid-state NMR in high-field gradients: prospects for imaging bone using the long echo-train summation technique (LETS). J Magn Reson 2001;151:235–41.
[20] Fernández-Seara MA, Wehrli SL, Wehrli FW. Multipoint mapping for imaging of semi-solid materials. J Magn Reson 2003;160:144–50.
[21] Wehrli FW, Fernández-Seara MA. Nuclear magnetic resonance studies of bone water. Ann Biomed Eng 2005;33:79–86.
[22] Brown CE, Battocletti JH, Srinivasan R, Allaway JR, Moore J, Sigmann P. In vivo 31P nuclear magnetic resonance spectroscopy of bone mineral for evaluation of osteoporosis. Clin Chem 1988;34:1431–8.
[23] Wolff SD, Chesnick S, Frank JA, Lim KO, Balaban RS. Magnetization transfer contrast: MR imaging of the knee. Radiology 1991;179:623–8.
[24] Kim DK, Ceckler TL, Hascall VC, Calabro A, Balaban RS. Analysis of water-macromolecule proton magnetization transfer in articular cartilage. Magn Reson Med 1993;29:211–5.
[25] Ceckler TL, Wolff SD, Yip V, Simon SA, Balaban RS. Dynamic and chemical factors affecting water proton relaxation by macromolecules. J Magn Reson 1992;98:637–45.
[26] Eng J, Ceckler TL, Balaban RS. Quantitative 1H magnetization transfer imaging in vivo. Magn Reson Med 1991;17:304–14.
[27] Gray ML, Burstein D, Lesperance LM, Gehrke L. Magnetization transfer in cartilage and its constituent macromolecules. Magn Reson Med 1995;34:319–25.
[28] Potter K, Butler J, Horton WE, Spencer RGS. Response of engineered cartilage tissue to biochemical agents as studied by proton MRI microscopy. Arthritis Rheum 2000;43:1580–90.
[29] Seo GS, Aoki J, Moriya H, Karakida O, Sone S, Hidaka H, et al. Hyaline cartilage: in vivo and in vitro assessment with magnetization transfer imaging. Radiology 1996;201:525–30.
[30] Laurent D, Wasvary J, Yin J, Rudin M, Pellas TC, O'Byrne E. Quantitative and qualitative assessment of articular cartilage in the goat knee with magnetization transfer imaging. Magn Reson Imaging 2001;19:1279–86.
[31] Potter K, Landis WJ, Spencer RGS. Histomorphometry of the embryonic avian growth plate by proton nuclear magnetic resonance microscopy. J Bone Miner Res 2001;16:1092–100.
[32] Potter K, Leapman RD, Basser PJ, Landis WJ. Cartilage calcification studied by proton nuclear magnetic resonance microscopy. J Bone Miner Res 2002;17:652–60.
[33] Kuhn LT, Wu Y, Rey C, Gerstenfeld LC, Grynpas MD, Ackerman JL, et al. Structure, composition, and maturation of newly deposited calcium-phosphate crystals in chicken osteoblast cell cultures. J Bone Miner Res 2000;15:1301–9.
[34] Carden A, Morris MD. Application of vibrational spectroscopy to the study of mineralized tissues (review). J Biomed Opt 2000;5:259–68.
[35] Boskey AL, Camacho NP, Mendelsohn R, Doty SB, Binderman I. FT-IR microscopic mappings of early mineralization in chick limb bud mesenchymal cell cultures. Calcif Tissue Int 1992;51:443–8.
[36] Boskey AL, Stiner D, Binderman I, Doty SB. Effects of proteoglycan modification on mineral formation in a differentiating chick limb-bud mesenchymal cell culture system. J Cell Biochem 1997;64:632–43.
[37] Paschalis EP, Betts F, DiCarlo E, Mendelsohn R, Boskey AL. FTIR microspectroscopic analysis of normal human cortical and trabecular bone. Calcif Tissue Int 1997;61:480–6.
[38] Paschalis EP, Betts F, DiCarlo E, Mendelsohn R, Boskey AL. FTIR microspectroscopic analysis of human iliac crest biopsies from untreated osteoporotic bone. Calcif Tissue Int 1997;61:487–92.
[39] Mendelsohn R, Hassankhani A, DiCarlo E, Boskey A. FT-IR microscopy of endochondral ossification at 20 μ spatial resolution. Calcif Tissue Int 1989;44:20–4.
[40] Marcott C, Reeder RC, Paschalis EP, Tatakis DN, Boskey AL, Mendelsohn R. Infrared microspectroscopic imaging of biomineralized tissues using a mercury–cadmium–telluride focal-plane array detector. Cell Mol Biol 1998;44:109–15.
[41] Tesch W, Eidelman N, Roschger P, Goldenberg F, Klaushofer K, Fratzl P. Graded microstructure and mechanical properties of human crown dentin. Calcif Tissue Int 2001;69:147–57.
[42] Petersen E, Potter K, Butler J, Fishbein KW, Horton WE, Spencer RGS, et al. Bioreactor and probe system for magnetic resonance microimaging and spectroscopy of chondrocytes and neocartilage. Int J Imaging Syst Technol 1997;8:285–92.
[43] Gerstenfeld LC, Chipman SD, Glowacki J, Lian JB. Expression of differentiated function by mineralizing cultures of chicken osteoblasts. Dev Biol 1987;122:49–60.
[44] Eidelman N, Simon Jr CG. Characterization of combinatorial polymer blend composition gradients by FTIR microspectroscopy. J Res Natl Inst Stand Technol 2004;109:219–31.
[45] Eidelman N, Tsutsumi N, Chiang CK. Micro FTIR mapping of nanometer ferroelectric polymer films. Macromol Rapid Commun 2006;27:558–62.
[46] Rafferty DW, Virnelson RC. A novel reflective FT-IR microscopy method. Spectroscopy 1997;12:42–4.
[47] Prophet EB, Mills B, Arrington JA, Sobin LH. Laboratory Methods in Histotechnology. Washington, DC: American Registry of Pathology; 1992. p. 128–30.
[48] Landis WJ, Glimcher MJ. Electron diffraction and electron probe microanalysis of the mineral phase of bone tissue prepared by anhydrous techniques. J Ultrastruct Res 1978;63:188–223.
[49] Krivanek OL, Friedman SL, Gubbens AJ, Kraus B. An imaging filter for biological applications. Ultramicroscopy 1995;59:267–82.
[50] Mayer J, Deininger C, Reimer L. Electron spectroscopic diffraction. In: Reimer L, editor. Transmission Electron Microscopy, vol. 71. Berlin: Springer-Verlag; 1995. p. 291–345.
[51] Rasband WS, Bright DS. NIH Image: a public domain image processing program for the Macintosh. Microbeam Anal Soc J 1995;4:137–49.
[52] Fiori CE, Swyt CR. NIST/NIH Desktop Spectrum Analyzer (DTSA), SRD-38. 2.5.0 ed. Gaithersburg, MD: National Institute of Standards and Technology; 1992.
[53] Pellegrino ED, Biltz RM. Mineralization in the chick embryo I. Monohydrogen phosphate and carbonate relationships during maturation of bone crystal complex. Calcif Tissue Int 1972;10:128–35.
[54] Lees S. Mineralization of type I collagen. Biophys J 2003;85:204–7.
[55] Hoshi K, Kemmotsu S, Takeuchi Y, Amizuka N, Ozawa H. The primary calcification in bones follows removal of decorin and fusion of collagen fibrils. J Bone Miner Res 1999;14:273–80.
[56] Hoshi K, Ejiri S, Ozawa H. Localizational alterations of calcium, phosphorus, and calcification-related organics such as proteoglycans and alkaline phosphatase during bone calcification. J Bone Miner Res 2001;16:289–98.
[57] Weidenbaum M, Foster RJ, Best BA, Saed-Nejad F, Nickoloff E, Newhouse J, et al. Correlating magnetic resonance imaging with the biochemical content of the normal human intervertebral disc. J Orthop Res 1992;10:552–61.